Efficient and Exact C-arm Cone-Beam Imaging for Axially Extended Field-of-View using the Ellipse-Line-Ellipse Trajectory

Zhicong Yu, Günter Lauritsch, Joachim Hornegger, Frédéric Noo

***Abstract*—C-arm computed tomography for axially long field-of-view is an important extension to the current C-arm 3D imaging capability and can be crucial in some intra-operative cases. Recently, a novel data acquisition geometry, i.e., the Ellipse-Line-Ellipse trajectory, was proposed for this new technique. It has been shown that this trajectory satisfies mechanical motion constraints of a C-arm system and provides excellent geometrical characteristics for cone-beam image reconstruction. This work makes good use of these characteristics and develops an efficient and exact image reconstruction scheme using the general CB-FBP reconstruction theory. We demonstrate this scheme by computer simulations with a modified FORBILD head phantom.**

I. Introduction

C-arm Computed Tomography (CT) is an innovative technique that allows a C-arm system to produce 3D images using a set of cone-beam (CB) projections. Clinical reports (e.g., [1]) have shown that this new technique is becoming more and more useful in the interventional room, such as neurovascular imaging, interventional procedure guidance and post-surgery assessment. These reports have demonstrated that C-arm CT can reduce treatment related complications and improve interventional efficacy and safety.

However, current C-arm CT uses a circular short scan for data acquisition, which limits the imaging ability along the axial direction, i.e., along the centerline of the patient table. This limitation has been reported in hepatic vascular imaging where the entire liver is of interest [1]. In general, the axial-short coverage limitation is an issue whenever imaging an axially-long organ is needed in intra-operative cases, e.g., the entire spine or the whole aorta. Hence, development of C-arm CT for axially extended field-of-view (FOV) is needed in the interventional room. For convenience, we call this new development as extended-volume C-arm CT.

Significant effort has been made to achieve the extended-volume C-arm CT [2]. Three data acquisition geometries were investigated, namely, the reverse helix [3], [4], the arc-extended-line-arc (AELA) [5] and the ellipse-line-ellipse (ELE) [6]. The major challenge of extended-volume C-arm CT is that the projection data are axially truncated due to limited detector size. To overcome this challenge, efficient and exact R-line based reconstruction algorithms are the best candidates; an R-line is a segment of line that connects two points on a connected source trajectory. However, the reverse helix cannot provide sufficient R-line coverage in the region-of-interest (ROI), hence exact and efficient cone-beam (CB) image reconstruction is difficult for the reverse helical trajectory. The AELA trajectory has sufficient R-line coverage, but it is not continuous and induces x-ray exposure pause. The ELE trajectory is continuous and has sufficient R-line coverage in the ROI. Therefore, it is the best candidate for extended-volume C-arm CT.

Geometrical characteristics of the ELE trajectory have been thoroughly studied in [6], [2], and efficient and exact image reconstruction scheme using the differentiated back-projection (DBP) algorithm has been proposed [7]. To reduce computational cost, the DBP method has to first perform image reconstruction on R-line surfaces and then data rebinning from R-line surfaces to Cartesian coordinate system. The former step increases implementation complexity and the latter step may cause unnecessary resolution loss. To overcome these problems, the filtered-back-projection (FBP)-type R-line based reconstruction algorithms are of interest.

This work aims at developing an efficient and exact image reconstruction scheme for the ELE trajectory based on the general CB-FBP reconstruction theory [8], [9], [10]. Although different reconstruction schemes have been proposed for various circle-plus trajectories [11], [12], none of them are readily applicable to the ELE trajectory. The scheme for a circle-plus-line trajectory [11] cannot solve the problem at hand, because an R-line of the ELE trajectory may involve two elliptical arcs and one line. The scheme for a general circle-plus trajectory [12] cannot be used neither: the ELE trajectory usually uses short scan due to mechanical motion constraints of a C-arm system, but this scheme requires the general circle to be closed. To apply the general CB-FBP theory to the ELE trajectory, a new reconstruction scheme needs to be developed.

This paper is organized as follows. First, in Section II, we describe the geometry of the ELE trajectory and clarify the criteria for ROI design. Next, in Section III, we review the general CB-FBP reconstruction theory and explain the new reconstruction scheme for the ELE trajectory. Then, we demonstrate the proposed reconstruction scheme in Section IV by computer simulations using a modified FORBILD head phantom. We conclude this work in Section V.

Z. Yu and F. Noo are with Department of Radiology, University of Utah, Salt Lake City, USA; G. Lauritsch is with Siemens AG, Healthcare Sector, Forchheim, Germany; J. Hornegger is with Pattern Recognition Lab, University of Erlangen-Nuremberg, Erlangen, Germany. This work was partially supported by a grant of Siemens AG, Healthcare Sector and by the U.S. National Institutes of Health (NIH) under grant R21 EB009168 and R01 EB007236. Its contents are solely the responsibility of the authors and do not necessarily represent the official views of the NIH. The concepts presented in this paper are based on research and are not commercially available.

II. ELE Trajectory

A. Geometry

The ELE trajectory lies on a cylindrical surface that is centered on the long-axis of the patient table as shown on the left of Figure 1. Without loss of generality, we will only consider one basic cycle of this trajectory, i.e., the bottom half of the left of Figure 1. For convenience, we will simply call this basic cycle the ELE trajectory in subsequent sections.

The ELE trajectory is composed of two elliptical arcs that are connected by a segment of line. We call these two elliptical arcs the upper and lower T-arcs, respectively, whereas the segment of line is called the T-line. In the attached (x, y, z) coordinate system, the ELE trajectory is centered on the z-axis and mirror symmetric relative to the (x, y)-plane. The T-arcs are perpendicular to the (x, z)-plane and the T-line is parallel to the z-axis; see the right of Figure 1.

Let λ and γ_m be a polar angle and a fan angle, respectively. We denote $\underline{a}_{\mathrm{u}}(\lambda)$ and $\underline{a}_{\mathrm{l}}(\lambda)$ as vertex points on the upper and lower T-arcs, respectively, and refer to $\underline{b}(z)$ as a vertex point on the T-line. Let R be the radius of the cylindrical surface. We refer to the z coordinate of the center of the upper (resp. lower) T-arc as H (resp. $-H$), and the z coverage of each T-arc as $2\Delta H$. Mathematically, any vertex points on this ELE trajectory can be expressed by one of the following equations

$$\begin{aligned}\underline{a}_{\mathrm{u}}(\lambda) &= (R\cos\lambda, R\sin\lambda, \mathcal{H}(\lambda))^T,\\ \underline{b}(z) &= (R\cos\gamma_m, -R\sin\gamma_m, z)^T,\\ \underline{a}_{\mathrm{l}}(\lambda) &= (R\cos\lambda, R\sin\lambda, -\mathcal{H}(\lambda))^T,\end{aligned}$$

where $\lambda \in [-\gamma_m, \pi+\gamma_m]$ and $z \in [-\mathcal{H}(\gamma_m), \mathcal{H}(\gamma_m)]$ with $\mathcal{H}(\lambda) = H + \Delta H\cos\lambda$. For more details, we refer to [6].

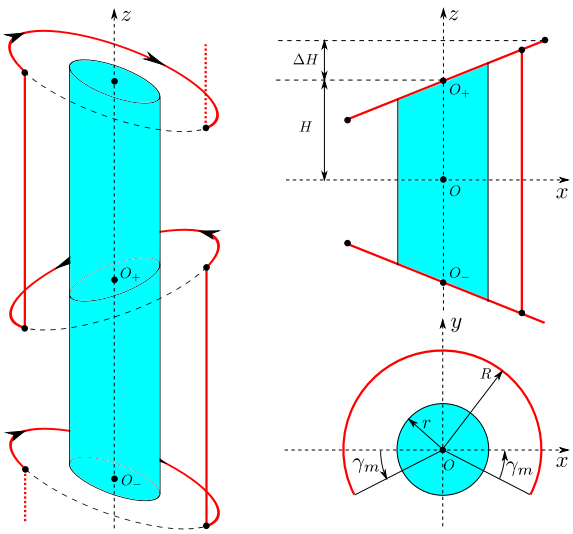

Fig. 1. Left: a complete ELE trajectory. We focus on one basic cycle: the bottom half of the trajectory on the left. Top right: orthogonal projection of the basic cycle of the ELE trajectory onto the (x, z)-plane. Bottom right: orthogonal projection of the basic cycle onto the (x, y)-plane. The light blue cylinder indicates the ROI.

B. ROI Design

There are three types of R-lines for the ELE trajectory: EL R-lines that connect the lower T-arc to the T-line, LE R-lines that connect the T-line to the upper T-arc, and EE R-lines that connect the two T-arcs. Let the radius of the region-of-interest (ROI) be r. According to [6], full R-line coverage in the ROI can be achieved by the following configurations:

$$\gamma_m = \arcsin(r/R) \quad \text{and} \quad \Delta H/H = r/R.$$

C. R-line Selection

For a given point of interest, there may be more than one R-line through it. In this work, we select the shortest R-line, as the same as that was used in [7]. The R-lines that are used for image reconstruction of the ROI that is inside the convex hull of the ELE trajectory and below the (x, y)-plane are shown in the left of Figure 2. These R-lines are either EL or EE, and they together provide full R-line coverage in the ROI; see the right of Figure 2. The ELE trajectory is mirror symmetric relative to the (x, y)-plane, so is the R-line coverage. Hence, the R-lines for image reconstruction of the ROI that is inside the convex hull and above the (x, y)-plane can be obtained similarly to those in Figure 2.

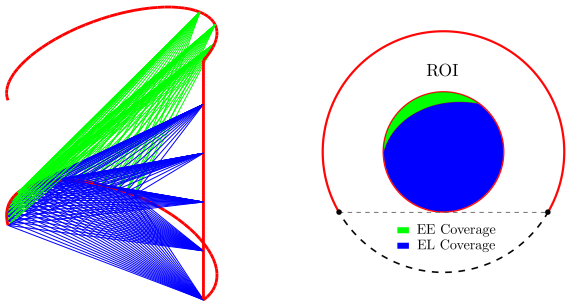

Fig. 2. Left: illustration of R-lines that are used for image reconstruction of the ROI that is inside the convex hull of the ELE trajectory and below the (x, y)-plane. Right: the R-line coverage of the ROI in the (x, y)-plane. Blue: EL R-lines; green: EE R-lines.

III. Reconstruction Method

A. General CB-FBP Reconstruction Theory

In this subsection, we review the general CB-FBP reconstruction theory [8], [9], [10]. We use the same notations as those were used in [10]. Let $\underline{a}(\lambda)$ be a point on a trajectory curve that starts from $\underline{a}(\lambda_{\mathrm{s}})$ and ends at $\underline{a}(\lambda_{\mathrm{e}})$. Let $\underline{a}'(\lambda)$ be the derivative of $\underline{a}(\lambda)$ with respect to λ, and let $\underline{x}$ be a point that is located on the line that connects $\underline{a}(\lambda_{\mathrm{s}})$ and $\underline{a}(\lambda_{\mathrm{e}})$. For illustration, see Figure 3. Let $\underline{e}_0$ be the unit vector pointing from $\underline{a}(\lambda)$ to $\underline{x}$, and let

$$\underline{e}_1 = \frac{\underline{a}'(\lambda) - (\underline{a}'(\lambda)\cdot\underline{e}_0)\underline{e}_0}{||\underline{a}'(\lambda) - (\underline{a}'(\lambda)\cdot\underline{e}_0)\underline{e}_0||} \quad \text{and} \quad \underline{e}_2 = \underline{e}_1 \times \underline{e}_0,$$

so that $\underline{e}_0$, $\underline{e}_1$ and $\underline{e}_2$ form a Cartesian coordinate system. In the plane that is spanned by $\underline{e}_1$ and $\underline{e}_2$, we define

$$\underline{e} = \cos\phi\,\underline{e}_1 + \sin\phi\,\underline{e}_2 \quad \text{and} \quad \underline{e}^{\perp} = \underline{e} \times \underline{e}_0,$$

where ϕ is the polar angle from $\underline{e}_1$ to $\underline{e}$ in the plane that is spanned by $\underline{e}_1$ and $\underline{e}_2$. Note that, when ϕ is identical to $\pi/2$ or $3\pi/2$, the plane spanned by $\underline{e}^{\perp}$ and $\underline{e}_0$ is tangent to the trajectory curve.

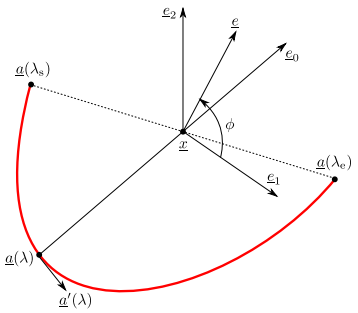

Fig. 3. Illustration for the general CB-FBP reconstruction theory.

Let $g(\lambda, \underline{x})$ be the line integral of the attenuation coefficients along the line that goes through $\underline{a}(\lambda)$ and $\underline{x}$, and let $g'(\lambda, \underline{x})$ be the derivative of $g(\lambda, \underline{x})$ with respect to λ. Now, consider an arbitrary Radon plane that contains $\underline{x}$ with normal $\underline{n}$. This plane intersects the trajectory curve (bounded by $\underline{a}_s$ and $\underline{a}_e$) at positions λ_1, λ_2, ... , $\lambda_{N(\underline{n},\underline{x})}$, with $N(\underline{n}, \underline{x})$ being the number of intersections. To address contributions of the projections corresponding to all these intersections, we introduce a weighting function, denoted as $M(\lambda, \phi; \underline{x})$, such that it satisfies the the equation below

$$\sum_{k=1}^{N(\underline{n},\underline{x})} M(\lambda_k, \phi_k; \underline{x}) = 1, \tag{1}$$

where ϕ has the same geometrical meaning as that in Figure 3. According to the general CB-FBP theory [8], [9], [10], $\underline{x}$ can be reconstructed by the formula below:

$$f(\underline{x}) = -\frac{1}{2\pi} \int_{\lambda_s}^{\lambda_e} \frac{g_{\mathrm{F}}(\lambda, \underline{x})}{||\underline{x} - \underline{a}(\lambda)||} \, d\lambda, \tag{2}$$

where

$$g_{\mathrm{F}}(\lambda, \underline{x}) = \int_0^{\pi} c(\lambda, \phi; \underline{x}) \, g_{\mathrm{H}}(\lambda, \phi, \underline{x}) \, d\phi, \tag{3}$$

with

$$c(\lambda, \phi; \underline{x}) = -\frac{1}{2} \left(\frac{\partial q}{\partial \phi} \right) (\lambda, \phi, \underline{x}), \tag{4}$$

$$q(\lambda, \phi; \underline{x}) = \mathrm{sign}(\cos\phi) M(\lambda, \phi; \underline{x}), \tag{5}$$

and

$$g_{\mathrm{H}}(\lambda, \phi, \underline{x}) = \int_{\pi}^{\pi} \frac{1}{\pi \, \sin\gamma'} g'(\lambda, \cos\gamma' \underline{e}_0 + \sin\gamma' \underline{e}^{\perp}) \, d\gamma'. \tag{6}$$

It is important to note that if $M(\lambda, \phi; \underline{x})$ is piecewise constant, $c(\lambda, \phi; \underline{x})$ will be a combination of pulse functions, which means only a finite filtering lines on the detector will be needed for reconstruction of $\underline{x}$.

B. Filtering Lines

Now, we focus on $M(\lambda, \phi; \underline{x})$, $c(\lambda, \phi; \underline{x})$, and the corresponding filtering lines. We denote the ROI that is inside the convex hull $\mathrm{ROI}_{\mathrm{C}}$, and refer to $\mathrm{ROI}_{\mathrm{U}}$ and $\mathrm{ROI}_{\mathrm{L}}$ as the portions of $\mathrm{ROI}_{\mathrm{C}}$ that are above and below the (x, y)-plane, respectively. For convenience, we only clarify our choice of $M(\lambda, \phi; \underline{x})$ and the corresponding filtering lines for $\mathrm{ROI}_{\mathrm{L}}$. Similar results can be obtained for $\mathrm{ROI}_{\mathrm{U}}$ due to the mirror symmetry of the ELE trajectory.

Let $\underline{x}$ be the point of interest, and let $\mathcal{R}(\underline{x})$ be the shortest R-line that goes through $\underline{x}$. We denote the trajectory curve that is bounded by $\mathcal{R}(\underline{x})$ as $\mathcal{S}(\underline{x})$. Let Π be a Radon plane that contains $\underline{x}$. By construction, there will be one or three intersections between $\mathcal{S}(\underline{x})$ and Π. In case that there is only one intersection, the value of $M(\lambda, \phi; \underline{x})$ is 1. In case that there are three intersections, we label them according to the order that the ELE trajectory goes through the plane, namely the first, second and third intersections. We design the $M(\lambda, \phi; \underline{x})$ according to the order of these intersections; see Table I. With the M function defined as in Table I, $c(\lambda, \phi; \underline{x})$ will be zero for most Radon planes, except for those tangent to the trajectory at the current view point or through the endpoints of $\mathcal{S}(\underline{x})$.

TABLE I
M FUNCTION USED FOR $\mathrm{ROI}_{\mathrm{L}}$

intersection order	M value
1st of three intersections	+1
2nd of three intersections	+1
3rd of three intersections	-1
1st of one intersection	+1

We select the filtering lines according to the M function defined in Table I. For this purpose, at each view point, we first project $\mathcal{S}(\underline{x})$ and the critical Radon planes onto the detector, and then study the value of $c(\lambda, \phi; \underline{x})$. Two types of R-lines may be associated to $\underline{x}$, i.e., EL R-lines and EE R-lines, depending on the location of $\underline{x}$. For an EL R-line, the projections of $\mathcal{S}(\underline{x})$ onto the detector when viewing from the lower T-arc and the T-line are illustrated in the left and right of Figure 4, respectively. It is observed that $c(\lambda, \phi; \underline{x})$ is none-zero only along $\mathcal{C}_1$ and $\mathcal{L}_1$, which are parallel and tangent to the projections of the lower T-arc, respectively.

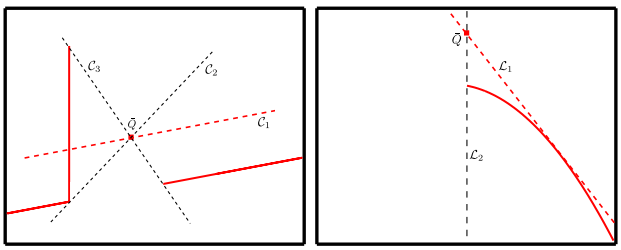

Fig. 4. Projections of an EL R-line segment onto the detector. Left: viewing from the lower T-arc; right: viewing from the T-line. Point $\bar{Q}$ is the projection of $\underline{x}$, and $c(\lambda, \phi; \underline{x})$ is zero everywhere except for $\mathcal{C}_1$ and $\mathcal{L}_1$.

For an EE R-line, when the view point is located on the lower T-arc, there are two cases regarding the relation between the filtering lines and the projection of $\mathcal{S}(\underline{x})$, as shown in Figure 5. However, in both cases, the filtering lines corresponding to none-zero $c(\lambda, \phi; \underline{x})$ are the same, namely $\mathcal{C}_1$, which is parallel to the projection of the lower T-arc. Similarly, when the view point is located on the T-line or on the upper T-arc, $c(\lambda, \phi; \underline{x})$ is zero everywhere except for the filtering lines that are tangent to the projections of the lower T-arc, as shown by $\mathcal{L}_1$ in Figure 6.

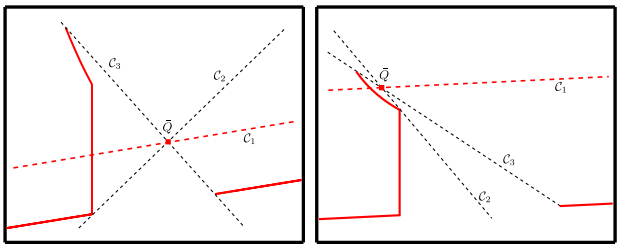

Fig. 5. Projections of an EE R-line segment onto the detector when the view point is located on the lower T-arc. Point $\bar{Q}$ is the projection of $\underline{x}$, and $c(\lambda, \phi; \underline{x})$ is zero everywhere except for $\mathcal{C}_1$.

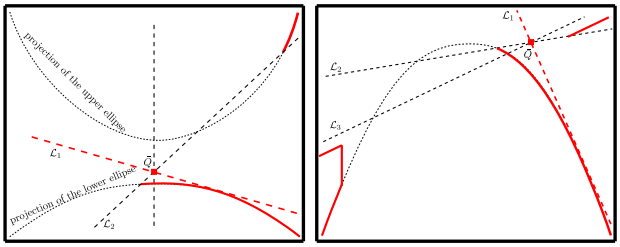

Fig. 6. Projections of an EE R-line segment onto the detector when the view point is located on the T-line (left) or on the upper T-arc (right). Point $\bar{Q}$ is the projection of $\underline{x}$, and $c(\lambda, \phi; \underline{x})$ is zero everywhere except for $\mathcal{L}_1$.

Based on the above analysis, for ROI_L, $g_\text{H}(\lambda, \phi, \underline{x})$ in Equation 6 should be calculated along the lines that are parallel to the projection of the lower T-arc when the view point is on the lower T-arc, and along the lines that are tangent to the projection of the lower T-arc when the view point is on the T-line or on the upper T-arc. It is important to note that the filtering lines $\mathcal{L}_1$ are drawn for illustration purpose. In reality, because the scan radius is much larger than the length of the T-line, the parabola is wide open and $\mathcal{L}_1$ is usually quite flat.

C. Reconstruction Scheme

The reconstruction scheme for ROI_L consists of three steps using the M function listed in Table I. They are: i) view-dependent differentiation, ii) Hilbert transform along $\mathcal{C}_1$ or $\mathcal{L}_1$, and iii) back-projection along R-line segments.

IV. Computer Simulation

We demonstrate our reconstruction scheme using a modified FORBILD head phantom [7]. The largest slice of this phantom is in disk shape at $z = 0\,\text{cm}$ of radius $12\,\text{cm}$. We adopted a plat panel detector with pixel size of $0.06\,\text{cm} \times 0.06\,\text{cm}$, a scan radius of $30\,\text{cm}$ and a source-to-detector of $45\,\text{cm}$. For the ELE trajectory, we chose $H = 5\,\text{cm}$, $\Delta H = 2\,\text{cm}$ and $\gamma_m = 24°$. For each T-arc, 500 CB projections were generated, whereas for the T-line, 61 CB projections were generated. All CB projections were acquired with quarter detector pixel shift, and each pixel value was calculated as the average of the values corresponding to 8 uniformly distributed sub-regions.

We performed image reconstruction according to Section III-C. For the view-dependent differentiation, we adopted the Noo's scheme [13], and selected 0.001 for the resolution control parameter ε. The reconstruction results are shown in Figure 7. For comparison, we also illustrate the reconstruction results obtained by only using the lower T-arc (Top right) and by using the lower T-arc and T-line together (bottom right). Compared to the result in the white box on the left, these results have significant CB artefacts. These results demonstrates the validity of the proposed reconstruction scheme.

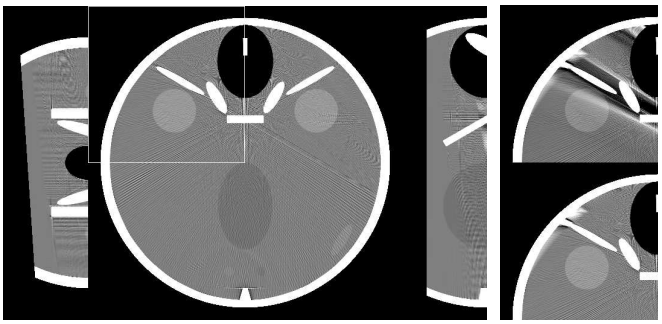

Fig. 7. Reconstruction results of the modified FORBILD head phantom. In the left figure, from left to right: coronal slice at $y = 6\,\text{cm}$; transverse slice at $z = 0\,\text{cm}$; sagittal slice at $x = 0\,\text{cm}$. In the right figure, from top to bottom: results using only the lower T-arc; results using the lower T-arc and the T-line together. Gray scale window: $[0, 100]\,\text{HU}$.

V. Conclusion and Discussion

We have proposed a reconstruction scheme for the ELE trajectory using the general CB-FBP theory. Computer simulation results show that efficient and exact C-arm long-object CB imaging is achievable using such a scheme.

The proposed reconstruction scheme avoids vertical filtering lines and thus allows data truncation in the axial direction. However, to what extent the truncation is allowed is not clear at this stage. This issue of detector requirement will be addressed in our future research.

References

[1] M. J. Wallace et al., "Three-dimensional C-arm cone-beam CT: applications in the interventional suite," *J. Vasc. Interv. Radiol.*, 2008.

[2] Z. Yu, "C-arm Computed Tomography with Extended Axial Field-of-View," Ph.D. dissertation, University of Erlangen-Nuremberg, 2013.

[3] S. Cho et al., "Exact reconstruction of volumetric images in reverse helical cone-beam CT," *Med. Phys.*, 2008.

[4] Z. Yu et al., "FDK-type reconstruction algorithms for the reverse helical trajectory," in *Proc. of MIC*. IEEE, 2011.

[5] Z. Yu et al., "Line plus arc source trajectories and their R-line coverage for long-object cone-beam imaging with a C-arm system," *Phys. Med. Biol.*, 2011.

[6] Z. Yu et al., "Ellipse-Line-Ellipse source trajectory and its R-line coverage for long-object cone-beam imaging with a C-arm system," in *Proc. of SPIE*, 2012.

[7] Z. Yu et al., "Extended-volume image reconstruction using the Ellipse-Line-Ellipse trajectory for a C-arm system," in *Proc. of Fully 3D*, 2013.

[8] A. Katsevich, "Theoretically exact FBP-type inversion algorithm for spiral CT," *SIAM J. Appl. Math.*, 2002.

[9] G.-H. Chen, "An alternative derivation of katsevichs cone-beam reconstruction formula," *Med. Phys.*, 2003.

[10] F. Noo, *Informatics in Medical Imaging*, ser. Imaging in Medical Diagnosis and Therapy, 2012, ch. 13 Principles of three-dimensional imaging from cone-beam projection data.

[11] A. Katsevich, "Image reconstruction for the circle and line trajectory," *Phys. Med. Biol.*, 2004.

[12] A. Katsevich, "Image reconstruction for a general circle-plus trajectory," *Inverse Problems*, 2007.

[13] F. Noo et al., "A new scheme for view-dependent data differentiation in fan-beam and cone-beam computed tomography," *Phys. Med. Biol.*, 2007.